

Water-Superstructured Solid Fuel Cells

Wei Zhang¹, Siyuan Fang¹, Hanrui Su¹, Wei Hao², Bohak Yoon², Gyeong S. Hwang², Kai Sun³,
Chung-Fu Chen⁴, Yu Zhu⁴, Yun Hang Hu^{1*}

Affiliations:

¹Department of Materials Science and Engineering, Michigan Technological University; Houghton, Michigan, 49931, United States.

²McKetta Department of Chemical Engineering, University of Texas at Austin; Austin, Texas, 78712, United States.

³Department of Materials Science and Engineering, University of Michigan; Ann Arbor, Michigan, 48109, United States.

⁴School of Polymer Science and Polymer Engineering, The University of Akron; Akron, Ohio, 44325, United States.

*Corresponding author. Email: yunhangh@mtu.edu

Abstract: Protonic ceramic fuel cells can be operated at low temperatures, but their performances relying on bulk ion transfer in solid electrolytes are usually limited by much lower proton conductivity than 0.1 S cm^{-1} below $600 \text{ }^\circ\text{C}$. Herein, however, we report a strategy for Al_2O_3 insulator to become a protonic superconductor, namely, in-situ generation of superstructured-water in porous Al_2O_3 layer could realize the unprecedented water-mediated proton transfer on Al_2O_3 surface, attaining ultrahigh proton conductivity of 0.13 S cm^{-1} at $550 \text{ }^\circ\text{C}$. With such a water-superstructured proton-superconductor, we created water-superstructured solid fuel cell, achieving very high power density of 1036 mW cm^{-2} and high open circuit voltage above 1.1 V at $550 \text{ }^\circ\text{C}$ with H_2 fuel. This provides a general approach to develop protonic superconductors and solid fuel cells.

Introduction

Fuel cells, which are an important type of energy devices, can overcome the limitations of fuel combustion efficiency. Compared with proton exchange membrane fuel cells that require expensive noble metal catalysts with poor tolerance to gas impurity, ceramic fuel cells offer a superior capability for power generation with fuel flexibility, high efficiency, and non-noble metal catalysts (*1–11*). The yttria-stabilized zirconia (YSZ)-based solid oxide fuel cells (SOFCs) represent the 1st generation ceramic cells, but their high operating temperature up to $1000 \text{ }^\circ\text{C}$ caused material compatibility issues and high cost (*12*). The development of new oxide-ion conducting electrolytes, such as gadolinium-doped ceria (GDC) and samarium-doped ceria (SDC), created the 2nd generation SOFCs with a decreased operating temperature of $600\text{--}700 \text{ }^\circ\text{C}$ (*13, 14*). The 3rd generation nanostructured SOFCs can be operated even at $450\text{--}600 \text{ }^\circ\text{C}$, but their performance declines rapidly with decreasing temperature owing to the high activation energy of oxide-ion conduction (*4, 14*). In contrast, protonic conduction in proton-conductive oxides, such as yttrium-doped barium zirconate (BZY), possesses a decreased activation energy, enabling protonic ceramic fuel cells (PCFCs) to be operated at a lower temperature and thus improving the sealing, durability, and cost (*15–19*). Nevertheless, conductivities of typical proton ceramic

electrolytes are still much smaller than 0.1 S cm^{-1} at a relatively low temperature ($< 600 \text{ }^\circ\text{C}$) (18, 20, 21), leading to much worse performance of PCFCs than that of high-temperature SOFCs and thus restricting the commercial application of PCFCs. Two technical approaches are being exploited to improve the proton conductivity for PCFCs. One is to reduce the electrolyte thickness, thus decreasing the proton transfer distance (7, 21). However, fabricating an ultrathin electrolyte film requires advanced techniques that unavoidably make mass production difficult and costly. Furthermore, it may cause “short circuits” due to electron conduction if the electrolyte film is too thin to ensure the isolation between the anode and the cathode. Another route is to modify current ceramic proton conductors and invent new materials, which is strongly determined by the progress of materials science and engineering (7, 21, 22).

As a breakthrough, Mavrikakis, Besenbacher and co-workers directly observed water-mediated proton diffusion on FeO surface by high-speed scanning tunneling microscopy (STM) (23). Furthermore, protons and water were found to be retained in the grain boundary or “internal surface” of nanograined YSZ, contributing to proton conductivity (24). The necessity of adsorbed water for fast proton conduction on sulfated zirconia was also reported (25). These suggest that the surface transfer of proton on a metal oxide is dependent on water-promotion instead of the intrinsic ionic bulk conductivity of the metal oxide. Therefore, as a hypothesis, we propose that the metal oxide ionic-insulator with condensed/adsorbed water (namely, superstructured water on a solid surface) would become a proton conductor via water-mediate proton surface diffusion. Because $\gamma\text{-Al}_2\text{O}_3$ is an ionic-insulator with excellent chemical and thermal stability (26) and remarkable affinity for water (27), we selected it to test this hypothesis. It was demonstrated that the Al_2O_3 can be changed from a ceramic insulator to a protonic superconductor by in-situ forming the superstructured-water in a porous Al_2O_3 layer for surface water-mediated proton transfer. Furthermore, with such a water-superstructured porous Al_2O_3 layer for fast proton transfer between the anode and the cathode, we created a new type of solid fuel cell—water-superstructured solid fuel cell (WSSFC), achieving a very high power output of 1036 mW cm^{-2} and high open circuit voltage (OCV) above 1.1 V when operated with H_2 as the fuel at $550 \text{ }^\circ\text{C}$.

Results and discussion

Design of WSSFC based on modeling and experimental observations

Water-mediated proton diffusion on metal oxide surfaces was experimental demonstrated (23-25), which has stimulated us to propose that water would be able to promote the surface transfer of protons on a metal oxide ionic-insulator. The feasibility of this hypothesis was examined by our density functional theory (DFT) calculations with Al_2O_3 as follows. First, a H_2O molecule was added to the (100) surface of $\gamma\text{-Al}_2\text{O}_3$ to form an adsorbed H_2O . Meanwhile, a proton was introduced to the Al_2O_3 and optimized to the stable state, at which the proton formed hydroxy groups with the O atoms bonded to the fourfold coordinated Al. The proton transfer on the surface of $\gamma\text{-Al}_2\text{O}_3$ with assistance of the adsorbed H_2O molecule was simulated based on the climbing image nudged elastic band (ci-NEB) method. The proton from the hydroxy group on the surface of $\gamma\text{-Al}_2\text{O}_3$ contacts the adsorbed H_2O molecule to generate the H_3O^+ transition state, which elongates and then breaks the O-H bond of the H_2O molecule to give a proton to the surface of $\gamma\text{-Al}_2\text{O}_3$ and thus form another hydroxy group (**Fig. 1A**). Overall, the process could be considered as a proton transfer from one to another O atom bonded with the fourfold coordinated Al with the assistance of the H_2O molecule via the H_3O^+ transition state. The energy barrier of the whole proton transfer process is 0.394 eV, which is much lower than that (1.019-1.215 eV) without water-

assistance (**fig. S1**). Furthermore, to reveal the effect of intermolecular hydrogen bonding between H₂O molecules on the proton transfer on the Al₂O₃ surface, the adsorbed H₂O molecule was replaced by a water monolayer (ML) consisting of 10 H₂O molecules (with intermolecular hydrogen bonding) on the surface of γ -Al₂O₃. **Fig. S2** shows the similar water-mediated proton transfer approach on the surface of Al₂O₃ via the H₃O⁺ transition state, and its proton transfer energy barrier (0.303 eV) is even lower than that (0.394 eV) with an adsorbed H₂O. Therefore, the energy barrier of proton transfer promoted either with the water ML or the adsorbed water molecule is lower than the activation barriers (0.4-0.6 eV) of reported excellent proton ceramic conductors (28). Furthermore, the energy barrier of water-mediated proton transfer is also smaller than the adsorption energy (0.514 eV) of ML H₂O molecule and that (0.642-0.813 eV) of independent H₂O molecule on Al₂O₃. These clearly demonstrate the feasibility of the fast water-mediated proton transfer on the surface of γ -Al₂O₃.

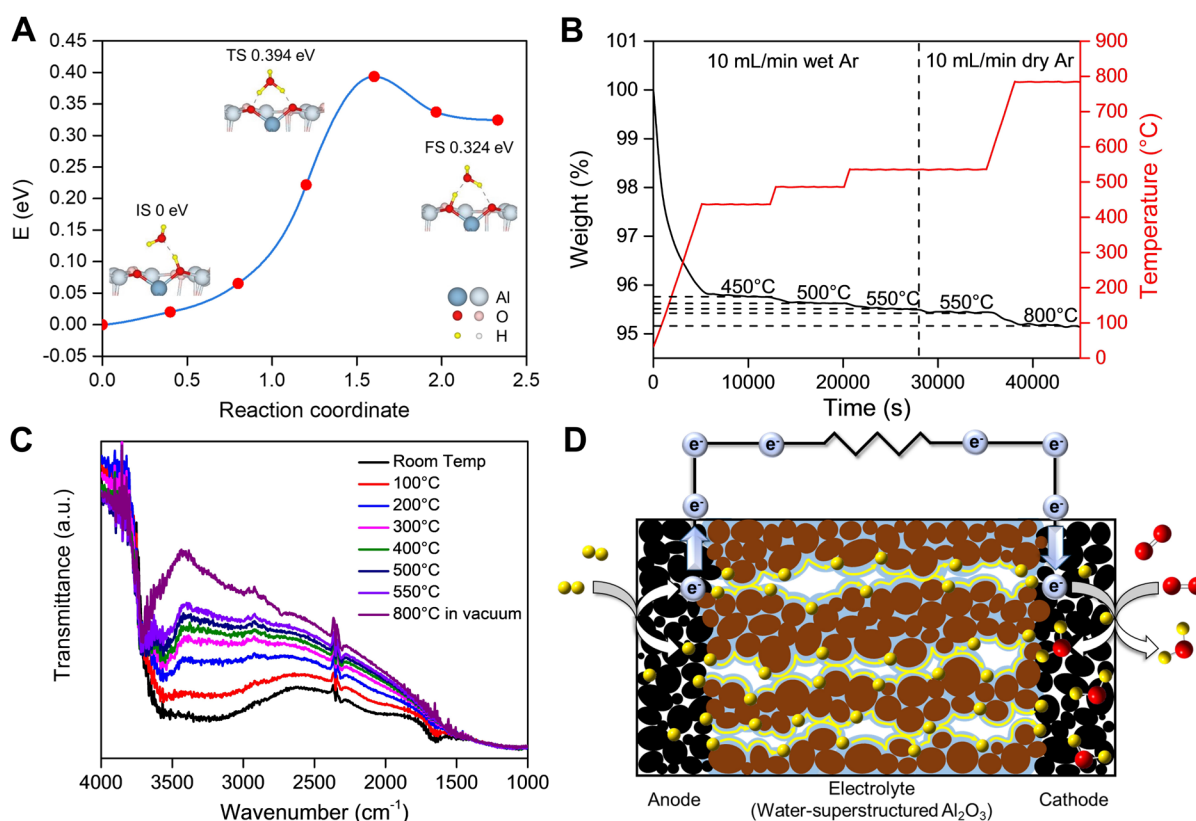


Fig. 1. Design of water-superstructured solid fuel cell (WSSFC). (A) Water-mediated proton transfer on Al₂O₃ surface with an adsorbed H₂O molecule demonstrated by DFT calculation. (B) Thermogravimetric curve of Al₂O₃ pellet (pressed at 100 MPa) in 3% H₂O/Ar atmosphere. (C) In-situ FT-IR spectra of Al₂O₃ at various temperatures in 3% H₂O/Ar atmosphere. (D) Schematic design of WSSFC (black for electrode material, brown for Al₂O₃, light blue for water, red for oxygen atom, and yellow for proton or hydrogen atom).

Water on surface of Al₂O₃ (with external surface area of 19 m² g⁻¹ and total BET surface area of 113 m² g⁻¹, **figs. S3-S5**) under H₂O/Ar atmosphere was evaluated by thermogravimetric (TG) analysis at elevated temperatures (**Fig. 1A** and **tables S1 and S2**). Although water on the

Al₂O₃ pellet (pressed at 100 MPa) decreased with increasing temperature (**Fig. 1B**), 4.05 mg g⁻¹ of water still retained on the Al₂O₃ surface in the 3% H₂O/Ar atmosphere even at 550 °C (**table S1**). When H₂O content in Ar atmosphere increased to 9%, water on the Al₂O₃ at 550 °C increased to 9.01 mg g⁻¹, which could cover 6 m² g⁻¹ surface area of Al₂O₃ that is 32% of its external surface (19 m² g⁻¹) (**table S2**). Furthermore, the water retained on Al₂O₃ was further supported by the in-situ diffuse reflectance infrared Fourier transform spectrum, namely, the strong and broad IR band between 1800-3800 cm⁻¹ was observed in the 3% H₂O/Ar atmosphere from room temperature to elevated temperatures (**Fig. 1C**). The broad IR band, which was widely used to identify the water on the surface of metal oxides (24, 29), further confirmed the existence of water on Al₂O₃ even at 550 °C. Such water on Al₂O₃ surface at an elevated temperature is the so-called superstructured-water.

From the above modeling and experimental observations, we propose a new type of fuel cell—water-superstructured solid fuel cell (WSSFC), in which a porous Al₂O₃ film with adsorbed water molecules as a water-superstructured electrolyte for fast surface water-mediated proton transfer from the anode to the cathode (**Fig. 1D**). The superstructured-water in porous Al₂O₃ film is in-situ formed and remained by the water continuously produced during the cell operation.

Fabrication, evaluation, and characterization of WSSFCs

Based on the above design, we fabricated the WSSFC with a simple one-step method: The powder with a sandwich distribution (LiNi_{0.8}Co_{0.15}Al_{0.05}O₂, γ -Al₂O₃, and LiNi_{0.8}Co_{0.15}Al_{0.05}O₂) was physically pressed with a pressure of 100 MPa at room temperature into three porous layers as a symmetric cell, in which the γ -Al₂O₃ layer was located between two LiNi_{0.8}Co_{0.15}Al_{0.05}O₂ (LNCA) electrodes. The sandwich structure of the cell was confirmed by scanning electron microscope (SEM) images (**Fig. 2A**), namely, the Al₂O₃ layer with about 0.3 mm thickness is between two LNCA electrode layers. The porous structure of the cell disk was quantitatively analyzed by X-ray computed tomography (CT) technique, namely, the porosities of two LNCA electrodes are 27-30%, while the layer of γ -Al₂O₃ possesses the porosity of about 26%, which are consistent with SEM measurements (**table S3**). The pore size distribution of the Al₂O₃ layer from N₂ adsorption-desorption isotherm measurement demonstrates the rich mesopores mainly in 2-40 nm (**fig. S6**), even though some macropores in the Al₂O₃ layer were also observed in the SEM image (**Fig. 2A**). In contrast, macropores at μ m level are dominant in the electrodes (**Fig. 2A**). Furthermore, the constitution of continuous channels from these pores in the Al₂O₃ layer was revealed by gas analysis, namely, H₂ fed to the anode was detected by on-line gas chromatography (GC) in the cathode side without cell operation at room temperature (**fig. S7A**). To test the electrochemical performance of the cell, H₂ and air flows were introduced into the anode and reduced cathode of the cell, respectively. At the beginning, H₂ and air react with each other due to their diffusion through the continuous channels and produce water at 550 °C. The produced water diffused into porous Al₂O₃ layer to form adsorbed water as the superstructured-water through the porous structure of the Al₂O₃ layer, creating a proton superconductive electrolyte (See more discussion in the next section). Such a water-superstructured cell exhibited excellent performance as shown by the polarization (I-V) and corresponding power output (I-P) curves at low operating temperatures of 450-550 °C (**Fig. 2B**). The high OCV values above 1.1 V were obtained. Furthermore, the device achieved the very high peak power density of 1036 mW cm⁻² at 550 °C, which is much larger than those (below 600 mW cm⁻²) of most reported PCFCs (28, 30, 31). Even when the operating temperature decreased to 525, 500, 475, and 450 °C, the high power densities of 920, 793, 631, and 454 mW cm⁻² were still obtained, respectively. The cell also exhibited

excellent stability. Although the cell showed slight performance decrease with operation time at 550 °C, its performance remained constant without degradation for 100 hours at 500 °C (Fig. 2C), which is comparable to the best stability of reported SOFCs and PCFCs (30, 31).

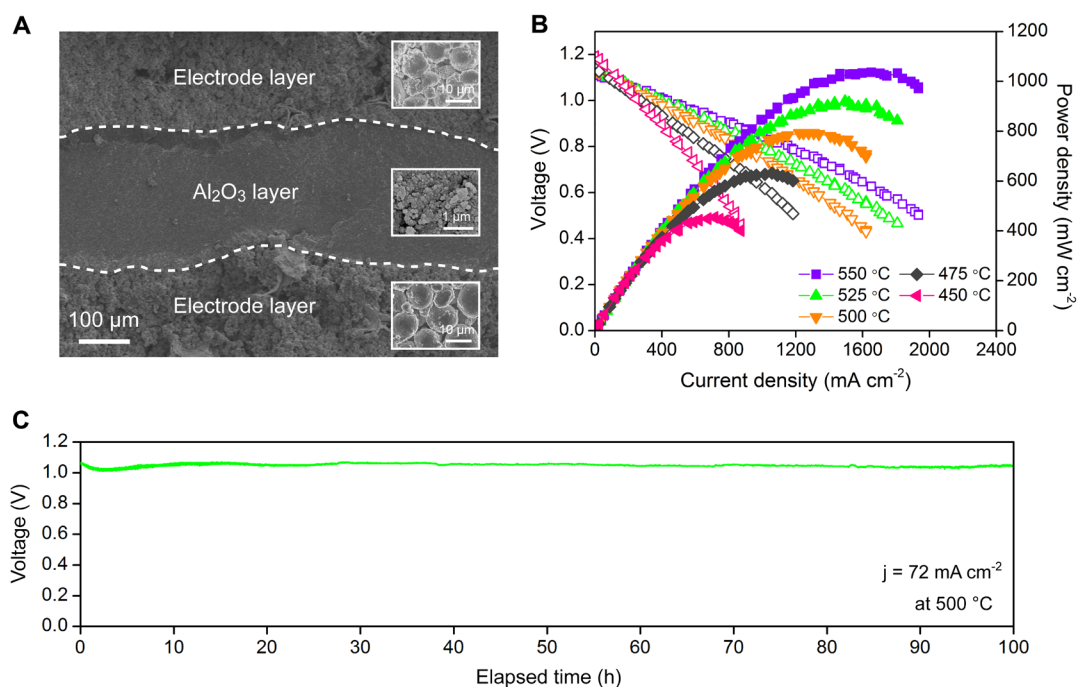


Fig. 2. Structure and electrochemical performance of water-superstructured solid fuel cell (WSSFC). (A) Cross-section SEM image of the fabricated cell with porous Al_2O_3 layer between two porous $\text{LiNi}_{0.8}\text{Co}_{0.15}\text{Al}_{0.05}\text{O}_2$ electrodes. (B) I-V and I-P curves of the WSSFC with H_2 fuel at 550–450 °C. (C) Stability evaluation at a constant current density at 500 °C for 100 hours.

Cell disk characterization and ion transfer evaluation of WSSFCs

The high OCV value above 1.1 V reveals the negligible electronic and mechanical leakage of the cell (Fig. 2B). Its negligible gas leakage was further confirmed by gas analysis (fig. S7B). In contrast, when we on-purpose drilled a hole (1 mm diameter) through the cell disk and thus created gas leakage (fig. S8), OCV decreased to almost zero (0.02 V). Therefore, the high OCV indicates the in-situ formation of a plugger in the porous cell disk to block gas diffusion between electrodes during the operation. This would be related to the LNCA electrodes because the replacement of LNCA with other electrodes resulted in zero OCV (table S4). Indeed, SEM images showed the denser interface (about 10 μm) between the anode and the Al_2O_3 layer (Fig. 3A) and the denser interface (about 8 μm) between the cathode and the Al_2O_3 layer (Fig. 3B). Compared to the electrodes and Al_2O_3 layer, the interfaces exhibited about 50% decrease in porosity (table S5). The in-situ produced water would easily plug narrower channels of the denser interfaces to block H_2 and O_2 gas diffusion in the cell disk during its operation. As a result, the direct reaction between H_2 and O_2 was greatly inhibited, and H_2 could be activated to generate protons and electrons at the anode in the cell. The produced electrons transfer through an external circuit to reach the cathode and reduce O_2 molecules into O^{2-} ions, while the generated protons fast transfer through the water-superstructured porous Al_2O_3 layer to react with O^{2-} ions at the Al_2O_3 -cathode

interface with the formation of water. Consequently, excellent performance with the high OCV value above 1.1 V was obtained for the cell.

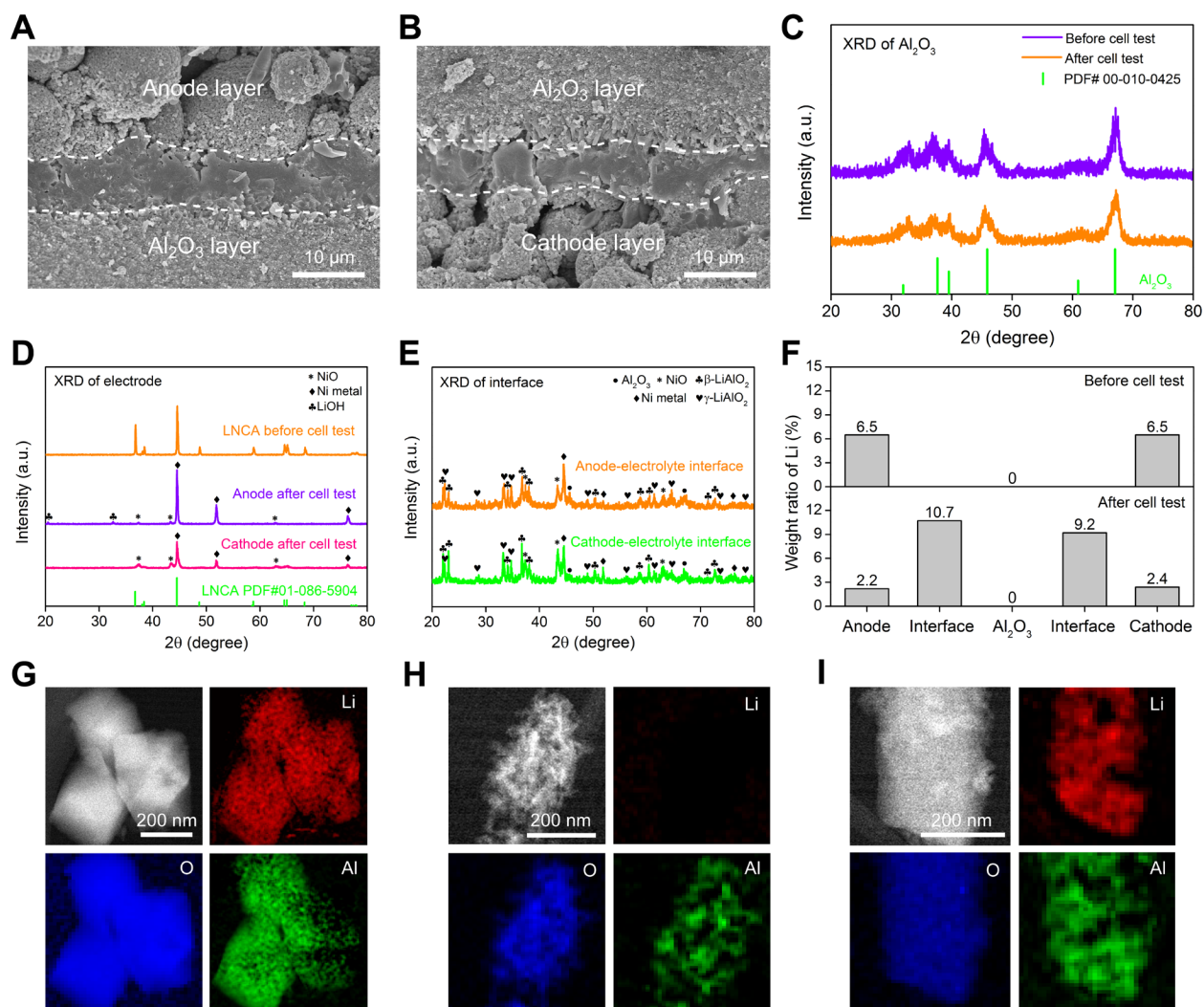


Fig. 3. Material characterization of WSSFC. SEM images of (A) anode-Al₂O₃ interface and (B) cathode-Al₂O₃ interface after cell test. XRD patterns of (C) Al₂O₃ layer, (D) electrodes, and (E) electrode-Al₂O₃ interfaces. (F) Weight ratio of Li in the cell materials from ICP-OES measurement. STEM-EELS elemental distributions of (G) anode-Al₂O₃ interface, (H) Al₂O₃ layer, and (I) cathode-Al₂O₃ interface after cell test.

The materials of the tested cell were deeply evaluated. X-ray diffraction (XRD) patterns revealed that the γ -Al₂O₃ crystal structure (PDF# 00-010-0425) of the Al₂O₃ layer remained unchanged (Fig. 3C), whereas the LNCA electrodes decomposed into Ni and NiO with strong peak intensity and LiOH with weak peak intensity after cell operation at 550 °C (Fig. 3D). The decomposition of LNCA electrodes was also reported for SOFCs with ion conductive electrolytes (such as SrTiO₃ and Gd_{0.1}Ce_{0.9}O_{1.95}) after cell operation with H₂ fuel at an elevated temperature (32–34). Furthermore, β -LiAlO₂ and γ -LiAlO₂ were detected by XRD with low crystalline in the two interfaces due to the reaction between LiOH (from the decomposition of LNCA) and Al₂O₃

(**Fig. 3E**), and such a reaction could inhibit Li^+ diffusion into the Al_2O_3 layer. The inductively coupled plasma (ICP) element analysis revealed the distribution of Li in the tested cell disk, namely, the Li contents of 2.2~2.4 wt% in the anode and cathode and about 9~10 wt% in the two interfaces, but zero in the middle Al_2O_3 layer (**Fig. 3F**). The Li state in the anode and cathode was identified as LiOH by X-ray photoelectron spectroscopy (XPS) (**fig. S9**). The existence of Li in the interfaces and its absence in the middle Al_2O_3 layer were further confirmed by electron energy-loss spectroscopy (EELS) mappings (**Figs. 3G, 3H, and 3I**) and XPS spectra (**fig. S10**). Therefore, the contribution of any Li ion-based compounds (such as LiOH, generated from the decomposition of LNCA electrodes) to the ionic conductivity of the Al_2O_3 layer is excluded in the cell. However, LiOH plays an important role in the cathode (**table S6** and **fig. S11** with detail discussion in supplementary material).

The excellent performance of the WSSFC was further supported by the following characterization of cell properties. The impedance plot shows the very low electrolyte resistance for the water-superstructured porous Al_2O_3 layer (**Fig. 4A**), leading to ultrahigh proton conductivity of 0.13 S cm^{-1} at $550 \text{ }^\circ\text{C}$ (**table S7**), which is much higher than reported values of proton conductors at the same temperature (28, 30, 31). The high proton conductivities of 0.11, 0.09, 0.08, and 0.07 S cm^{-1} were also obtained at 525, 500, 475, and $450 \text{ }^\circ\text{C}$, respectively (**Fig. 4B**, **table S7**, and **fig. S13**). Although the intrinsic Al_2O_3 is a well-known ionic insulator, the water-superstructured porous Al_2O_3 layer is responsible for the fast proton transfer. This was supported by the in-situ TG and FTIR analysis, which demonstrated the appreciable amount of water on Al_2O_3 surface (as super-structured water) in the H_2O -containing atmosphere at elevated temperatures up to $550 \text{ }^\circ\text{C}$ (**Figs. 1B and 1C**). Furthermore, the correlation between the proton conductivity and the operating temperature of the water-superstructured porous Al_2O_3 layer revealed a small activation energy of 0.343 eV for proton transfer (**Fig. 4B**), which is well consistent with the energy barriers (0.303~0.394 eV) of H_2O -mediated proton transfer on Al_2O_3 surface from the DFT calculations (**Fig. 1A** and **fig. S2**). In this proton transfer mechanism, the proton exchange between the surface OH group of Al_2O_3 and the H_2O molecule via the H_3O^+ transition state plays an important role. To experimentally confirm the proton exchange, liquid H_2O was dropped on Al_2O_3 to ensure the sufficient formation of surface OH groups at room temperature, followed by dropping liquid D_2O and then increasing temperature. As shown in **Fig. 4C**, one can see the broad IR band of condensed H_2O between 2800 and 3800 cm^{-1} and the broad one of condensed D_2O between 1700 and 2500 cm^{-1} . Furthermore, the stretching band (centered at 2730 - 2770 cm^{-1}) of OD group of Al_2O_3 started to occur at $200 \text{ }^\circ\text{C}$ and its IR intensity increased with increasing temperature, clearly demonstrating the D-H exchange between OH of Al_2O_3 and D of D_2O . The participation of OH groups of Al_2O_3 in the proton transfer was further supported by XPS spectra, namely, the content of surface OH group in the Al_2O_3 increased from 21.3% to 44.3% after the cell operation (**Fig. 4D**), indicating the bonding of protons to the surface O atoms of Al_2O_3 . These provide the strong evidences for the water-mediated proton transfer via the H_3O^+ transition state in the water-superstructured Al_2O_3 layer at elevated temperatures. This transition state could be further supported by the reported observation, in which H_3O^+ -like transition state was found in the water-mediated diffusion of proton on a FeO film by STM at room temperature or below (23), which revealed its fundamental difference from the Grötthaus mechanism that a proton transfers via a “water wire” in the liquid water phase (35). The high stability of the γ - Al_2O_3 layer in the water-superstructured cell was demonstrated by XPS spectra, XRD patterns, and TEM images, namely, the Al valence (**Fig. 4E**), the crystal structure (**Fig. 3C**), and the particle shape and size (25 nm) (**Fig. 4F**) of the γ - Al_2O_3 layer remained unchanged after the cell operation.

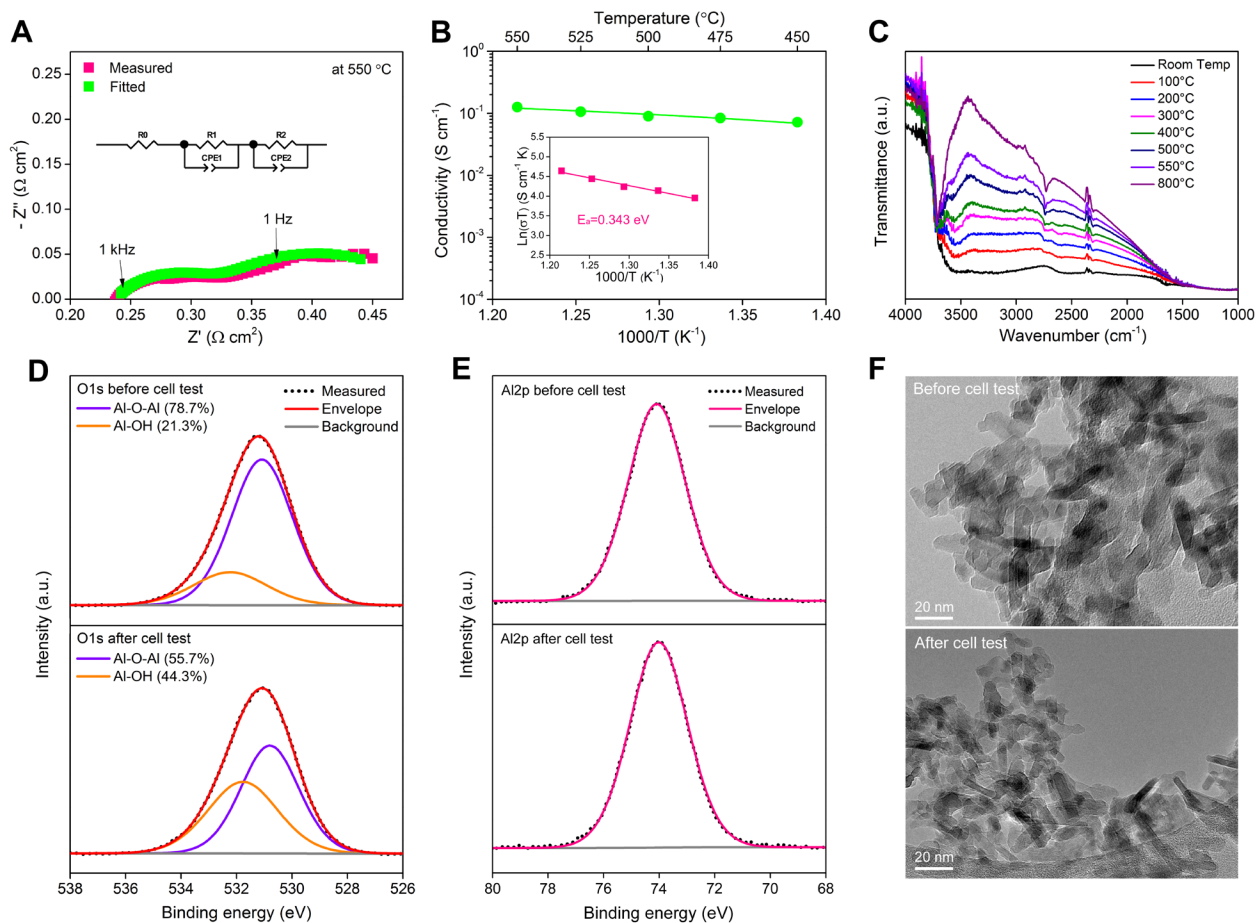


Fig. 4. Characterization of water-superstructured Al_2O_3 layer. (A) Nyquist plots of the water-superstructured porous Al_2O_3 -based fuel cell under H_2/air open-circuit conditions. (B) Proton conductivity of water-superstructured porous Al_2O_3 layer vs. temperature. (C) In-situ FT-IR spectra of condensed H_2O and D_2O over Al_2O_3 at various temperatures. (D) $\text{O}1\text{s}$ XPS spectra of Al_2O_3 before and after the cell test at 550°C . (E) $\text{Al}2\text{p}$ XPS spectra of Al_2O_3 before and after the cell test at 550°C . (F) TEM images of Al_2O_3 before and after the cell test at 550°C .

Effects of compacting pressure and Al_2O_3 layer thickness on cell performance

The compacting-pressure effect of fabricating a cell disk on its performance was examined. As shown in **Fig. 5A**, the peak power density decreased from 1036 to 207 mW cm^{-2} with increasing the fabrication compacting-pressure from 100 to 1500 MPa . This can be attributed to the decrease in proton conductivity (**Fig. 5B**), which is due to the diminished porosity (**fig. S14**). However, a relatively low compacting-pressure of 50 MPa also exhibited a lower peak power density (943 mW cm^{-2}) than that with 100 MPa , indicating that the pressure of 50 MPa is insufficient to compact Al_2O_3 particles close enough for the formation of the superstructured water at the interface between the particles, which is supported by its lower proton conductivity compared with that using 100 MPa (**Fig. 5B**). Therefore, the optimized compacting pressure for the cell fabrication is 100 MPa . Furthermore, the cell performance and the Al_2O_3 proton conductivity are also dependent on the thickness of the Al_2O_3 layer with 0.3 mm as the ideal one (**Fig. 5C and 5D**). Different from the conventional PCFCs that require more expensive proton conductors and complicated fabrication procedures, the WSSFC using water-superstructured porous Al_2O_3 layer as an unusual proton

conductor can be easily fabricated with the powders of γ - Al_2O_3 and the electrode material (LNCA) via one-step pressing process at 100 MPa. This can greatly reduce the cell cost.

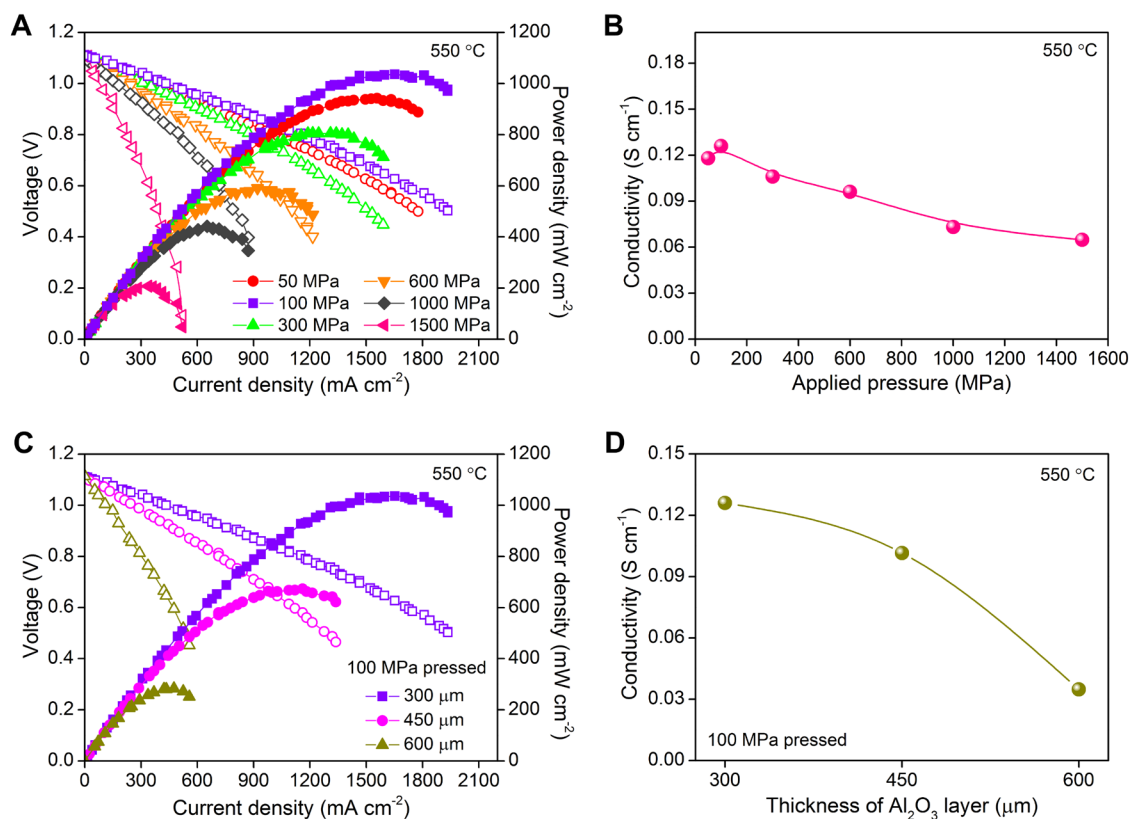


Fig. 5. Effect of WSSFC fabrication compacting pressure on its performance. (A) I-V and I-P curves of WSSFCs (fabricated with various compacting pressures from 50 to 1500 MPa) with H_2 fuel at 550 °C. **(B)** Proton conductivity of water-superstructured porous Al_2O_3 layer vs. its fabrication compacting pressure. **(C)** I-V and I-P curves of WSSFCs with various thicknesses of the Al_2O_3 layer with H_2 fuel at 550 °C. **(D)** Proton conductivity of water-superstructured porous Al_2O_3 layer vs. its thickness.

Conclusion

This work demonstrated a new type of fuel cell—the water-superstructured solid fuel cell (WSSFC), in which the in-situ generated water-superstructured porous Al_2O_3 layer plays as an unprecedented superconductive electrolyte for fast proton transfer. The WSSFC exhibited very high power densities of 1036 mW cm^{-2} at 550 °C and 454 mW cm^{-2} at 450 °C as well as high OCV above 1.1 V when operated with H_2 as the fuel. It would be promising for commercial applications due to its excellent performance, easy fabrication, and low cost. Furthermore, the in-situ formation of superstructured-water in porous metal oxide films would be a general strategy to develop protonic superconductors and solid fuel cells.

References and Notes

1. E. P. Murray, T. Tsai, S. A. Barnett, A direct-methane fuel cell with a ceria-based anode. *Nature* **400**, 649–651 (1999).
2. S. Park, J. M. Vohs, R. J. Gorte, Direct oxidation of hydrocarbons in a solid-oxide fuel cell. *Nature* **404**, 265–267 (2000).
3. T. Hibino *et al.*, A low-operating-temperature solid oxide fuel cell in hydrogen-air mixture. *Science* **288**, 2031–2033 (2000).
4. C. Duan *et al.*, Readily processed protonic ceramic fuel cells with high performance at low temperatures. *Science* **349**, 1321–1326 (2015).
5. Y. Zhang *et al.*, Thermal-expansion offset for high-performance fuel cell cathodes. *Nature* **591**, 246–251 (2021).
6. J. Myung, D. Neagu, D. N. Miller, J. T. S. Irvine, Switching on electrocatalytic activity in solid oxide cells. *Nature* **537**, 528–531 (2016).
7. C. Duan *et al.*, Highly durable, coking and sulfur tolerant, fuel-flexible protonic ceramic fuel cells. *Nature* **557**, 217–222 (2018).
8. Z. Shao *et al.*, A thermally self-sustained micro solid-oxide fuel-cell stack with high power density. *Nature* **435**, 795–798 (2005).
9. T. Suzuki *et al.*, Impact of anode microstructure on solid oxide fuel cells. *Science* **325**, 852–855 (2009).
10. E. D. Wachsman, K. T. Lee, Lowering the Temperature of solid oxide fuel cells. *Science* **334**, 935–939 (2011).
11. L. Yang *et al.*, Enhanced sulfur and coking tolerance of a mixed ion conductor for SOFCs: $\text{BaZr}_{0.1}\text{Ce}_{0.7}\text{Y}_{0.2-x}\text{Yb}_x\text{O}_{3-\delta}$. *Science* **326**, 126–129 (2009).
12. T. A. Adams II, J. Nease, D. Tucker, P. I. Barton, Energy conversion with solid oxide fuel cell systems: A review of concepts and outlooks for the short- and long-term. *Ind. Eng. Chem. Res.* **52**, 3089–3111 (2012).
13. A. J. Jacobson, Materials for Solid Oxide Fuel Cells. *Chem. Mater.* **22**, 660–674 (2009).
14. H. Su, Y. H. Hu, Progress in low-temperature solid oxide fuel cells with hydrocarbon fuels. *Chem. Eng. J.* **402**, 126235 (2020).
15. S. Choi *et al.*, Exceptional power density and stability at intermediate temperatures in protonic ceramic fuel cells. *Nat. Energy* **3**, 202–210 (2018).
16. D. Pergolesi *et al.*, High proton conduction in grain-boundary-free yttrium-doped barium zirconate films grown by pulsed laser deposition. *Nat. Mater.* **9**, 846–852 (2010).
17. P. Babilo, T. Uda, S. M. Haile, Processing of yttrium-doped barium zirconate for high proton conductivity. *J. Mater. Res.* **22**, 1322–1330 (2007).
18. P. Babilo, S. M. Haile, Enhanced Sintering of Yttrium-Doped Barium Zirconate by Addition of ZnO. *J. Am. Ceram. Soc.* **88**, 2362–2368 (2005).
19. K. D. Kreuer *et al.*, Proton conducting alkaline earth zirconates and titanates for high drain electrochemical applications. *Solid State Ion.* **145**, 295–306 (2001).

20. I. H. Kim *et al.*, Determination of partial conductivities and computational analysis of the theoretical power density of BaZr_{0.1}Ce_{0.7}Y_{0.1}Yb_{0.1}O_{3-δ} (BZCYYb1711) electrolyte under various PCFC conditions. *J. Mater. Chem. A* **7**, 21321–21328 (2019).
21. Y. Zhou *et al.*, Strongly correlated perovskite fuel cells. *Nature* **534**, 231–234 (2016).
22. K. D. Kreuer, Proton-conducting oxides. *Annu. Rev. Mater. Res.* **33**, 333–59 (2003).
23. L. R. Merte *et al.*, Water-mediated proton hopping on an iron oxide surface. *Science* **336**, 889–893 (2012).
24. S. Miyoshi *et al.*, Low-temperature protonic conduction based on surface protonics: An example of nanostructured yttria-doped zirconia. *Chem. Mater.* **26**, 5194–5200 (2014).
25. S. Hara, M. Miyayama, Proton conductivity of superacidic sulfated zirconia. *Solid State Ionics* **168**, 111–116 (2004).
26. J. Pappis, W. D. Kingery, Electrical properties of single-crystal and polycrystalline alumina at high temperatures, *J. Amer. Ceram. Soc.*, **44**, 459–464(1961).
27. S. Cai *et al.*, Possible Dual-Charge-Carrier Mechanism of Surface Conduction on γ -Alumina, *J. Phys. Chem. C* **111**, 5506–5513 (2007).
28. Y. Meng *et al.*, Review: recent progress in low-temperature proton-conducting ceramics. *J. Mater. Sci.* **54**, 9291–9312 (2019).
29. P. A. Thiel, T. E. Madey, The interaction of water with solid surfaces: Fundamental aspects. *Surf. Sci. Rep.* **7**, 211–385 (1987).
30. S. S. Shin *et al.*, Multiscale structured low-temperature solid oxide fuel cells with 13 W power at 500 °C. *Energy Environ. Sci.* **13**, 3459–3468 (2020).
31. W. Zhang, Y. H. Hu, Progress in proton-conducting oxides as electrolytes for low-temperature solid oxide fuel cells: From materials to devices. *Energy Sci. Eng.* **9**, 984–1011 (2021).
32. Y. He *et al.*, Mechanism for major improvement in SOFC electrolyte conductivity when using lithium compounds as anode, *ACS Appl. Energy Mater.* **3**, 4134–4138 (2020).
33. G. Chen *et al.*, Electrochemical mechanisms of an advanced low-temperature fuel cell with a SrTiO₃ electrolyte, *J. Mater. Chem. A* **7**, 9638–9645 (2019).
34. R. Lan, S. Tao, Novel proton conductors in the layered oxide material Li_xIAI_{0.5}Co_{0.5}O₂. *Adv. Energy Mater.* **4**, 1301683 (2014).
35. Z. Luz, S. Meiboom, The Activation Energies of Proton Transfer Reactions in Water. *J. Am. Chem. Soc.* **86**, 4768–4769 (1964).

Acknowledgments:

Funding:

U.S. National Science Foundation grant CMMI-1661699 (WZ, SF, HS, YHH)

Author contributions:

YHH developed the intellectual concept, designed the fuel cell structure, and provided supervisory guidance on the experiments. WZ prepared materials, fabricated fuel cells, tested

cell performances, and conducted characterizations of EIS, GC, XRD, SEM, and TEM. SF conducted the measurements of in-situ FTIR and AFM as well as TG, the determination of surface areas and pore size distributions, and the quantitative analysis of XPS spectra and SEM images. HS explored electrode materials. WH, BY and GSH conducted the DFT computational work with deep analysis. KS conducted the measurements of XPS and STEM-EELS. CC and YZ conducted the X-ray computed tomography analysis of cell disks. All contributed to the data analysis. YHH wrote the manuscript with input from all other authors.

Competing interests:

YHH, WZ, and SF are named as inventors in US patent application on water-superstructured solid fuel cells (WSSFCs) submitted by Michigan Technological University on June 16, 2021.

Data and materials availability:

All data are available in the main text or the supplementary materials.

Supplementary Materials

Materials and Methods

Figs. S1 to S15

Tables S1 to S7

Supplementary Materials for

Water-Superstructured Solid Fuel Cells

Wei Zhang¹, Siyuan Fang¹, Hanrui Su¹, Wei Hao², Bohak Yoon², Gyeong S. Hwang², Kai Sun³,
Chung-Fu Chen⁴, Yu Zhu⁴, Yun Hang Hu^{1*}

Correspondence to: yunhangh@mtu.edu

This PDF file includes:

Materials and Methods
Figs. S1 to S15
Tables S1 to S7

Materials and Methods

Materials and fuel cell disk fabrication

The commercial ultra-pure grade γ -Al₂O₃ powder (99.99%, Inframat Advanced Materials) was thermally treated at 900 °C in air for 10 h. The LiNi_{0.8}Co_{0.15}Al_{0.05}O₂ (LNCA) powder (NEI Corporation) was used as the electrode material, which was mixed with terpineol, coated on one side of Ni-foam and dried at 80 °C for 24 h to obtain LNCA electrode pieces. Fuel cell devices were fabricated by a simple dry-pressing method. Namely, one LNCA electrode piece, the γ -Al₂O₃ powder, and another LNCA electrode piece were layer-by-layer put into a steel die to form a symmetric LNCA/Al₂O₃/LNCA configuration, and then uniaxially compacted into a cylindrical porous disk. The applied pressure for the compaction ranged from 50 to 1500 MPa. All the produced cell disks have an active area of 0.64 cm² with thickness of 1-1.5 mm. Notably, although the cell disk does not possess a typical electrolyte, the Al₂O₃ layer between the two electrodes will be activated by in-situ produced water during the cell operation, forming water-superstructured Al₂O₃ layer as a proton superconductive electrolyte (see next section).

Electrochemical performance tests of water-superstructured fuel cells

A fuel cell disk was mounted and sealed on a custom-designed testing holder for performance tests. Ultra-high-purity hydrogen (99.999%, 60-80 ml min⁻¹) and ambient air (~100 ml min⁻¹) were used as fuel and oxidant at 1 atmosphere, respectively. Both the electrodes were in-situ reduced by hydrogen at 550 °C for 0.5 h before performance tests. During the cell operation, the in-situ produced water can be adsorbed on the surface of Al₂O₃ to create the water-superstructured Al₂O₃ layer as the proton superconductive electrolyte. I-V (current-voltage) and I-P (current-power) characteristics were measured by a programmable DC electronic load (IT8511A+, TEquipment). The gas leaking was tested by on-line gas chromatography (Hewlett Packard 5890 Series II equipped with an Alltech Porapak Q column and a thermal conductivity detector).

The electrical conductivity of the electrolyte was evaluated by electrochemical impedance spectra (EIS) in H₂/air atmospheres. The data were recorded by an electrochemical workstation (CHI760E, CH Instruments) under open-circuit conditions from 10⁶ to 0.1 Hz, with an amplitude of 10 mV at temperatures ranged from 450 to 550 °C. The measured data were fitted by the ZSimpWin 3.60 software (Ametek Scientific Instruments) to identify the electrolyte and the electrode process. The activation energy (E_a) was calculated with the following equation:

$$\sigma = \frac{A}{T} \exp\left(\frac{-E_a}{kT}\right) \quad (1)$$

where σ is the measured conductivity, T the absolute temperature, k the Boltzmann constant, and A the pre-exponential factor.

Basic characterizations of materials and devices

Phase crystal structure of powder samples was examined by the Scintag XDS2000 X-Ray powder diffractometer (XRD). Morphological and component analysis were conducted by the Hitachi S-4700 field emission scanning electron microscope (FE-SEM) and the FEI 200 kV Titan Themis scanning transmission electron microscope (STEM). The porous structure of the cell disk was evaluated by X-ray computed tomography (CT) technique with a Skyscan 1172 μ CT instrument (under 59 kV, 169 μ A and 10 W with a 0.5 mm Al filter) and its porosity was calculated with the CTan software. The N₂ adsorption-desorption isotherm, total BET surface area, and pore size distribution were measured on a Micromeritics ASAP 2000 adsorption instrument at 77 K. Before measurement, the samples were degassed in vacuum at 120 °C for 8 h. Furthermore, the three-dimensional morphology and size of Al₂O₃ particles were acquired on an Asylum Research

MFP-3D Origin+ atomic force microscope (AFM) working in the tapping mode with the 1-nm silicon probe. One hundred Al₂O₃ particles were imaged for statistical analysis of the external surface area. The chemical states of Al₂O₃ and LNCA were characterized by a PHI 5800 X-ray photoelectron spectrometer (XPS) with Mg source anode. All binding energies were calibrated with respect to the C1s line of adventitious carbon at 284.6 eV. STEM-EELS (scanning transmission electron microscopy-electron energy loss spectroscopy) images and mappings were obtained with A JEOL-JEM 3100R05 cold-FEG TEM equipped with both probe and imaging aberration correctors. The microscope was operated at 300 keV in STEM mode. The lens setting that defines a probe size smaller than 1 Å was used. EELS spectra were collected using a K2 camera using STEM EELS SI mode.

Thermogravimetric analysis

The thermogravimetric analysis of Al₂O₃ pellets was carried out using the Mettler Toledo TGA/SDTA851e system. Before the measurement, Al₂O₃ pellet (~40 mg) was pretreated at 400 °C for 3 h. Afterwards, Al₂O₃ was subjected to 10 ml min⁻¹ water-saturated Ar gas (i.e., about 3% H₂O/Ar) flow with the temperature rise from 25 to 550 °C at 5 °C min⁻¹. The temperature was held at 450, 500, and 550 °C for 2 h respectively for reaching the adsorption-desorption equilibrium. Then, 10 ml min⁻¹ dry Ar gas flow was introduced to the analyzer at 550 °C for 2 h, followed by 800 °C for another 2 h to get the absolute weight of Al₂O₃.

In-situ Fourier-transform infrared spectroscopy

Fourier-transform infrared spectroscopy (FTIR) was carried out on a Shimadzu IRAffinity-1 spectrometer with an in-situ diffuse reflection cell (DiffusIR, PIKE Technologies) which is equipped with a ZnSe window and can be heated up to 800 °C. To investigate the water adsorption ability of Al₂O₃ at elevated temperatures, Al₂O₃ in a porous ceramic cup was subjected to 10 ml min⁻¹ water-saturated Ar gas (i.e., about 3% H₂O/Ar) flow at room temperature, followed by heating with rate of 2 °C min⁻¹ to selected temperatures (25, 100, 200, 300, 400, 500, and 550 °C), each of which was kept for 1 hour to ensure the water adsorption-desorption equilibrium before recording spectra. The FTIR spectra were collected in the region from 1000 to 4000 cm⁻¹. Afterwards, Al₂O₃ was heated from 550 to 800 °C at 2 °C min⁻¹ in vacuum and maintained at 800 °C for 12 h to obtain the reference spectrum without any water. The amount of water adsorbed on Al₂O₃ at each selected temperature was determined from the in-situ FTIR spectrum in the range from 1500 to 4000 cm⁻¹.

Furthermore, to elucidate the role of the hydroxyl group of Al₂O₃ in proton transfer, isotope exchange experiment with the use of deuterated water (D₂O, 99.9 atom% D, Sigma-Aldrich) was carried out. Namely, after pressing Al₂O₃ into the ceramic cup, 3 droplets of water (H₂O) were dripped onto the Al₂O₃. Then, after 20-min stabilization to ensure all the Al₂O₃ surface to be covered by H₂O and the sufficient formation of surface hydroxyl groups, 3 droplets of D₂O were dripped onto the H₂O-covered Al₂O₃, followed by heating from 25 to 100, 200, 300, 400, 500, and 550 °C in vacuum at 2 °C min⁻¹ and held at each of these temperatures for 1 h before collecting the spectra. Afterwards, the temperature was elevated to 800 °C to acquire the spectrum without any H₂O and D₂O.

Inductively coupled plasma-optical emission spectroscopy (ICP-OES)

The accurate contents of Li in 5 parts of the used cell disk (the anode, the anode-Al₂O₃ interface, the middle Al₂O₃ layer, the cathode-Al₂O₃ interface, and the cathode) were determined

by a PerkinElmer Optima 7000DV inductively coupled plasma-optical emission spectrometer (ICP-OES). To ensure the dissolution of Li, all the samples were previously treated by aqua regia for 3 days.

Calculation methods

The proton transfer calculations were performed on the basis of density functional theory (DFT) within the generalized gradient approximation (GGA), as implemented in the Vienna ab initio simulation package (VASP) (S1). The projector augmented wave (PAW) method with a plane wave basis set was employed to describe the interaction between the core and valence electrons. The valence configurations employed to construct the ionic pseudopotentials are $3s^23p^1$ for Al, $2s^22p^4$ for O and $1s^1$ for H. An energy cutoff of 450 eV was applied for the plane wave expansion of the electronic eigenfunctions. For the Brillouin zone integration, we used a $(3\times3\times3)$ Monkhorst-Pack mesh of k points to determine the optimal geometries and total energies of the γ - Al_2O_3 bulk and $(1\times1\times1)$ Monkhorst-Pack mesh of k points for γ - Al_2O_3 (100) surface with a monolayer (ML) of H_2O . Reaction pathways and barriers were determined using the climbing image nudged elastic band (ci-NEB) method with five intermediate images for each elementary step.

The unit cell of pristine γ - Al_2O_3 bulk was constructed based on the data of work done by Digne et al (S2). A $2\times1\times1$ slab structure with a 15 Å vacuum was set up to simulate the (100) surface of γ - Al_2O_3 . Totally 10 H_2O molecules, which formed a ML of H_2O , were added on the top surface of γ - Al_2O_3 . An additional proton was inserted in the ML of H_2O and optimized to the stable state. For all slab structures, the atoms were fully relaxed with the conjugate gradient method until residual forces on all of the constituent atoms became smaller than 2×10^{-2} eV/Å. The similar model was used for evaluation of proton transfer on the (100) surface of γ - Al_2O_3 with an adsorbed H_2O molecule, but the water ML consisting of 10 H_2O molecules was replaced by single H_2O molecule.

Structure and property characterization of γ -Al₂O₃
DFT calculations for path and barrier of proton transfer

Fig. S1.

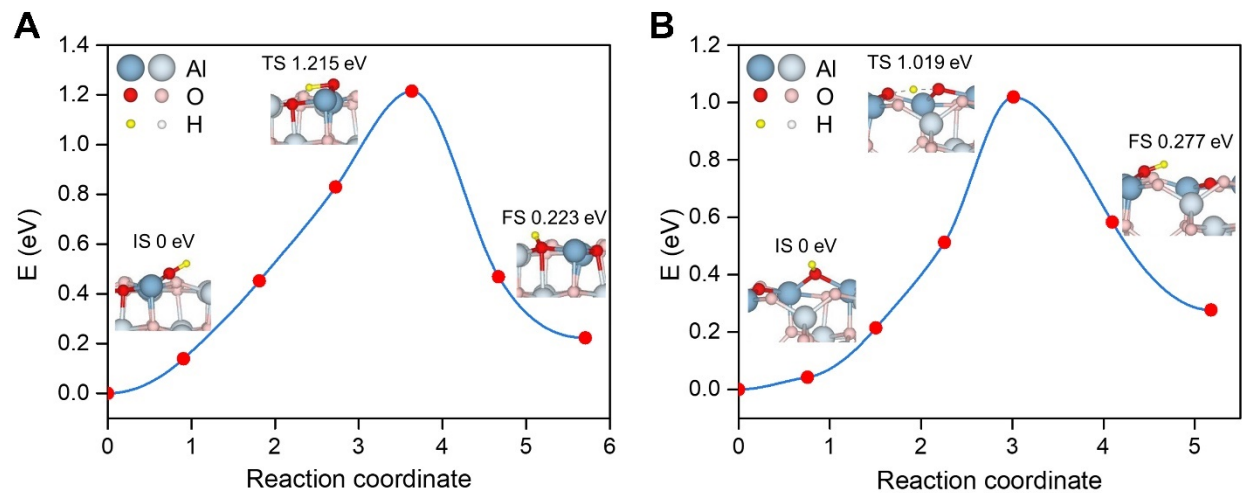


Fig. S1. Reaction path and barrier of proton transfer on the (100) surface of γ -Al₂O₃ for two most possible cases (A) and (B). The insertion figures show the initial, transition and final states of the proton transfer.

Fig. S2.

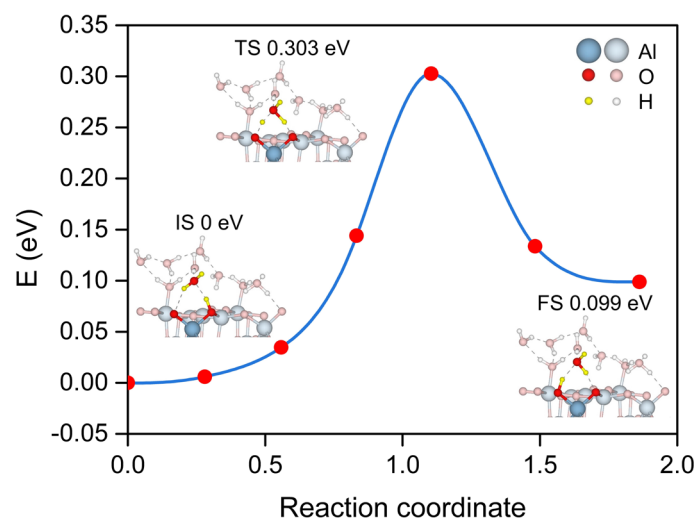


Fig. S2. Water-mediated proton transfer on Al₂O₃ surface with a water monolayer demonstrated by DFT calculation.

AFM image of γ -Al₂O₃ particles

Fig. S3.

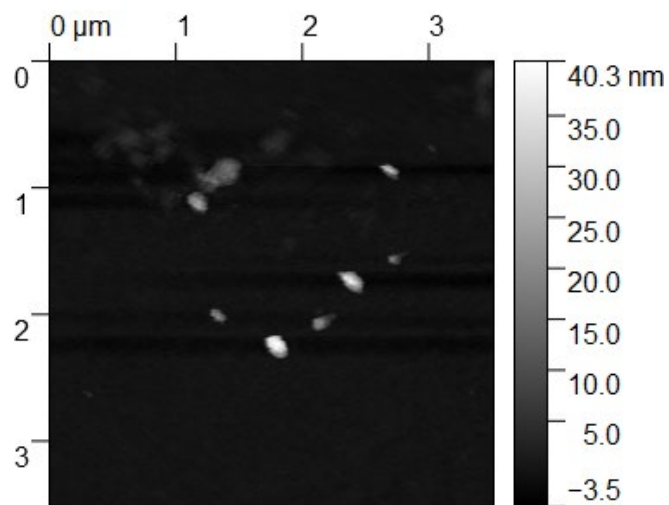


Fig. S3. AFM image of Al₂O₃ particles.

Fig. S4.

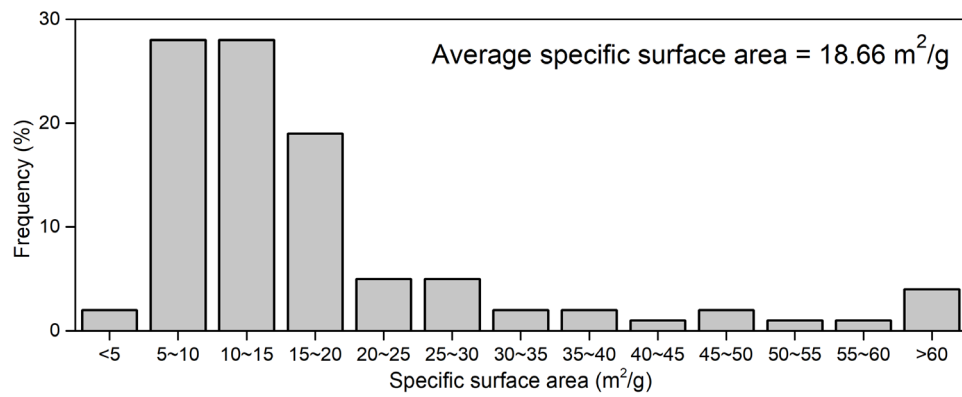


Fig. S4. Specific external surface area distribution of γ -Al₂O₃ powder from AFM images.

BET surface area and pore distribution of γ -Al₂O₃ powder

Fig. S5.

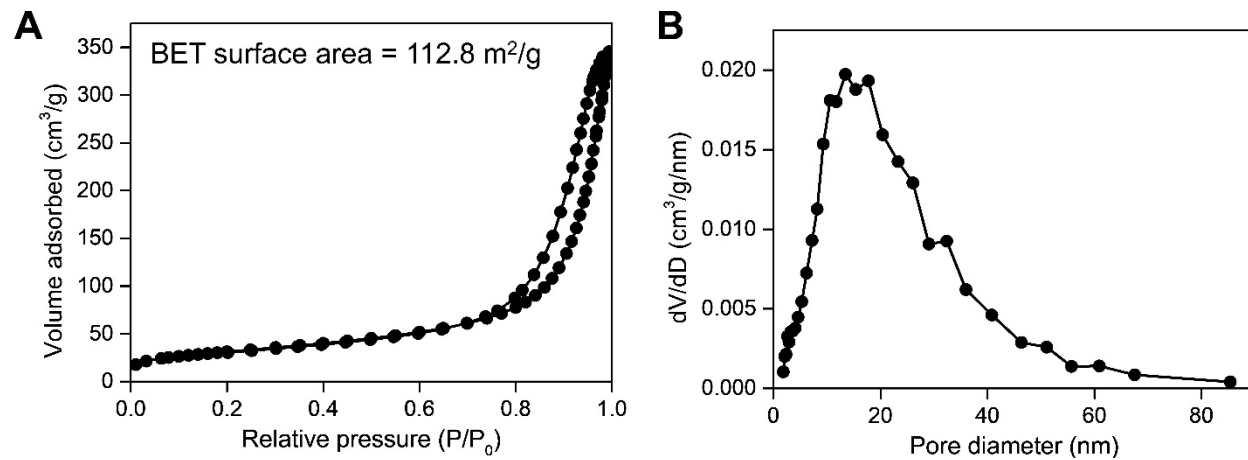


Fig. S5. Total surface area and pore structure of Al₂O₃ powder. **(A)** N₂ adsorption-desorption isotherm curves at liquid nitrogen temperature (-196 °C) and BET surface area. **(B)** BJH pore size distribution.

Thermogravimetric (TG) evaluation of water on γ -Al₂O₃ pellets

Table S1.

Table S1. Water coverage on Al₂O₃ pellet (fabricated by pressing Al₂O₃ powder) under 3% H₂O/argon flow from TG measurements.

Al₂O₃ pellet fabrication	Water adsorption on Al₂O₃ pellet		
Pressing pressure (MPa)	Temperature (°C)	Adsorbed water (mg H₂O/g Al₂O₃)	Water coverage area (m² H₂O/g Al₂O₃)
50	450	7.63	5.10
50	500	5.99	4.01
50	550	4.36	2.92
100	450	6.48	4.33
100	500	4.86	3.25
100	550	4.05	2.71
1500	450	5.48	3.67
1500	500	3.99	2.67
1500	550	2.99	2.00

Table S2.

Table S2. Water coverage on Al₂O₃ pellet (fabricated by pressing Al₂O₃ powder at 100 MPa) from TG measurements at 550 °C.

Water concentration in argon flow	Adsorbed water (mg H₂O/g Al₂O₃)	Water coverage area (m² H₂O/g Al₂O₃)
3%	4.05	2.71
9%	9.01	6.02

Characterization of WSSFC fabricated with 100 MPa compacting pressure
Porosities of electrodes and Al₂O₃ layer from 3D X-ray CT and SEM images

Table S3.

Table S3. Porosity of electrodes and Al₂O₃ layer.

Material	Porosity from 3D X-ray CT	Porosity from SEM
Top electrode	27.3%	26.1 %
Al ₂ O ₃ layer	26.3%	25.4%
Bottom electrode	29.8%	28.3%

BET surface area and pore distribution of γ -Al₂O₃ pellet

Fig. S6.

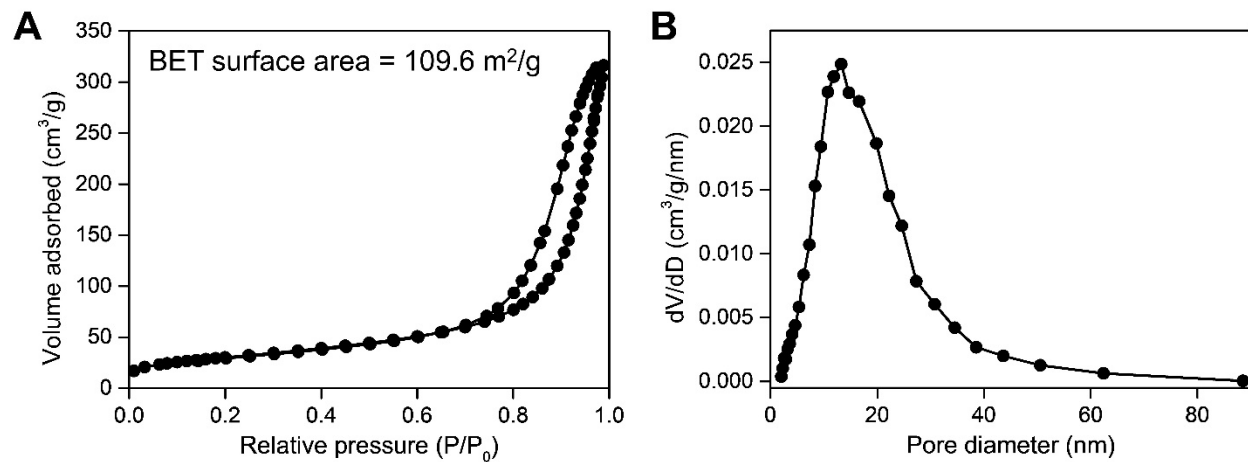


Fig. S6. Total surface area and pore structure of Al₂O₃ pellet. (A) N₂ adsorption-desorption isotherm curves at liquid nitrogen temperature (-196 °C) and BET surface area. (B) BJH pore size distribution.

Gas leakage test for a cell disk without a drilled hole

To confirm the diffusion of gas through the Al_2O_3 layer between the anode and the cathode, H_2 and air were introduced into the anode and cathode sides, respectively. As shown in **fig. S7A**, H_2 fed to the anode was detected by Gas Chromatography (GC) in the cathode side without cell operation at room temperature, revealing that H_2 transferred through the Al_2O_3 layer. In contrast, when the cell was being operated at $550\text{ }^\circ\text{C}$, H_2 peak almost disappeared in the GC spectrum (**fig. S7B**), indicating the negligible gas transfer through the Al_2O_3 layer during the cell operation, which is consistent with the obtained high open circuit voltage (OCV) of 1.11 V.

Fig. S7.

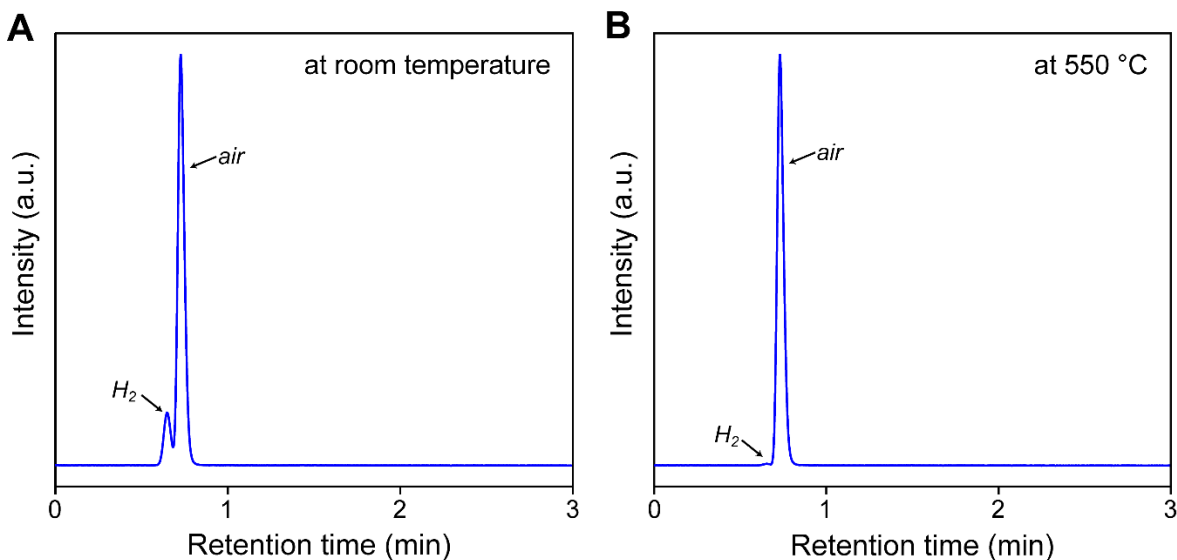


Fig. S7. GC spectra of gases in the cathode side of the LNCA/ γ - Al_2O_3 /LNCA cell, in which H_2 and air were respectively introduced into its anode and cathode (**A**) at room temperature (cell OCV: 0 V) and (**B**) at $550\text{ }^\circ\text{C}$ (cell OCV: 1.11 V).

Effect of gas leakage on OCV for a cell disk with a drilled hole

To evaluate the effect of gas leakage on OCV, we on-purpose drilled a hole (1 mm diameter) in the cell disk, thus the large H_2 peaks were observed in the GC spectra for both cases with and without operation, confirming the gas diffusion through the Al_2O_3 layer even during the operation at 550 °C (**fig. S8**) and thus leading to a negligible OCV of 0.02 V. This clearly demonstrated that the gas leakage in a cell can tremendously decrease its OCV.

Fig. S8.

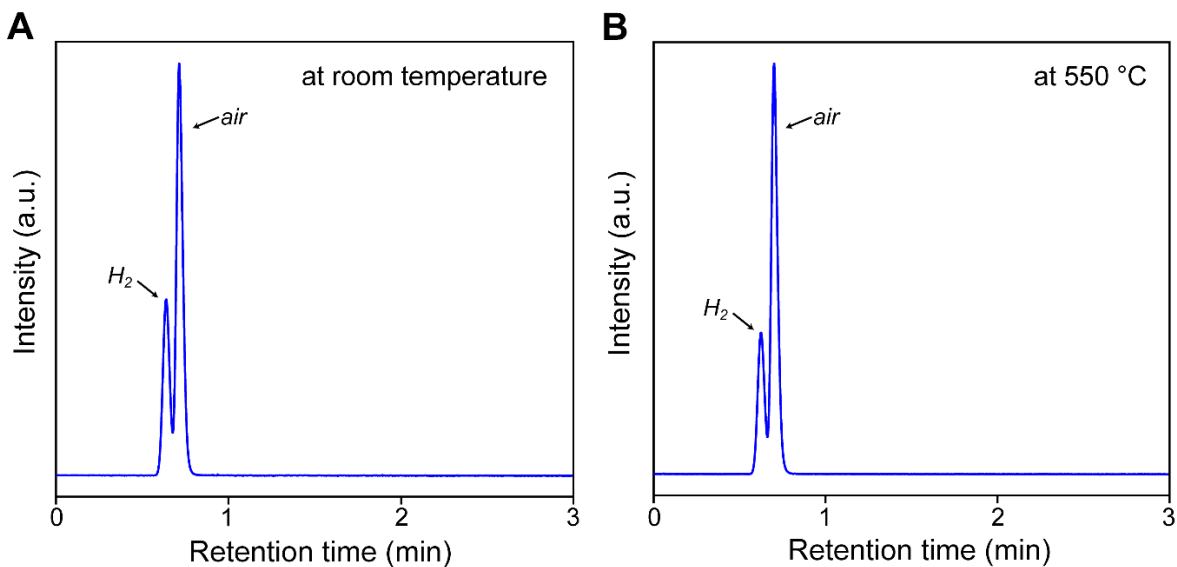


Fig. S8. GC spectra of gases in the cathode side of the LNCA/ γ - Al_2O_3 /LNCA cell with a drilled hole (1 mm hole diameter) through the cell disk, in which H_2 and air were respectively introduced into its anode and cathode (**A**) at room temperature (cell OCV: 0 V) and (**B**) at 550 °C (cell OCV: 0.02 V).

Exploration of electrodes

Table S4.

Table S4. Tests of anodes and cathodes for the WSSFC fed with H₂ fuel for anode and air for cathode at 550 °C.

Anode	Electrolyte	Cathode	Peak Power Density (mW/cm ²)	OCV (V)
NiO	Al ₂ O ₃	LSCF	0	0
Ni-SDC	Al ₂ O ₃	LSCF	0	0
Ni-BZCYYb	Al ₂ O ₃	LSCF	0	0
LNCA	Al ₂ O ₃	LSCF	0	0.34
NiO	Al ₂ O ₃	BCFZY	0	0
Ni-SDC	Al ₂ O ₃	BCFZY	0	0
Ni-BZCYYb	Al ₂ O ₃	BCFZY	0	0
LNCA	Al ₂ O ₃	BCFZY	0	0.76
NiO	Al ₂ O ₃	NiO	0	0
Ni-SDC	Al ₂ O ₃	NiO	0	0
Ni-BZCYYb	Al ₂ O ₃	NiO	0	0
LNCA	Al ₂ O ₃	NiO	0	0.41
NiO	Al ₂ O ₃	LNCA	50	0.78
Ni-SDC	Al ₂ O ₃	LNCA	181	0.74
Ni-BZCYYb	Al ₂ O ₃	LNCA	212	0.78
LNCA	Al ₂ O ₃	LNCA	1036	1.11

Note: SDC: Ce_{0.8}Sm_{0.2}O_{1.9}; BZCYYb: BaZr_{0.1}Ce_{0.7}Y_{0.1}Yb_{0.1}O_{3-δ}; LSCF: (La_{0.60}Sr_{0.40})_{0.95}Co_{0.20}Fe_{0.80}O_{3-δ}; BCFZY: BaCo_{0.4}Fe_{0.4}Zr_{0.1}Y_{0.1}O_{3-δ}; LNCA: LiNi_{0.8}Co_{0.15}Al_{0.05}O₂.

Porosities of electrodes, Al₂O₃ layer, and interfaces after cell test

Table S5.

Table S5. Porosities of electrodes, Al₂O₃ layer, and interfaces after cell test (from SEM images).

Material	Porosity
Anode	28.1%
Anode-Al ₂ O ₃ interface	13.2%
Al ₂ O ₃ layer	26.3%
Cathode-Al ₂ O ₃ interface	15.0%
Cathode	28.8%

Fig. S9.

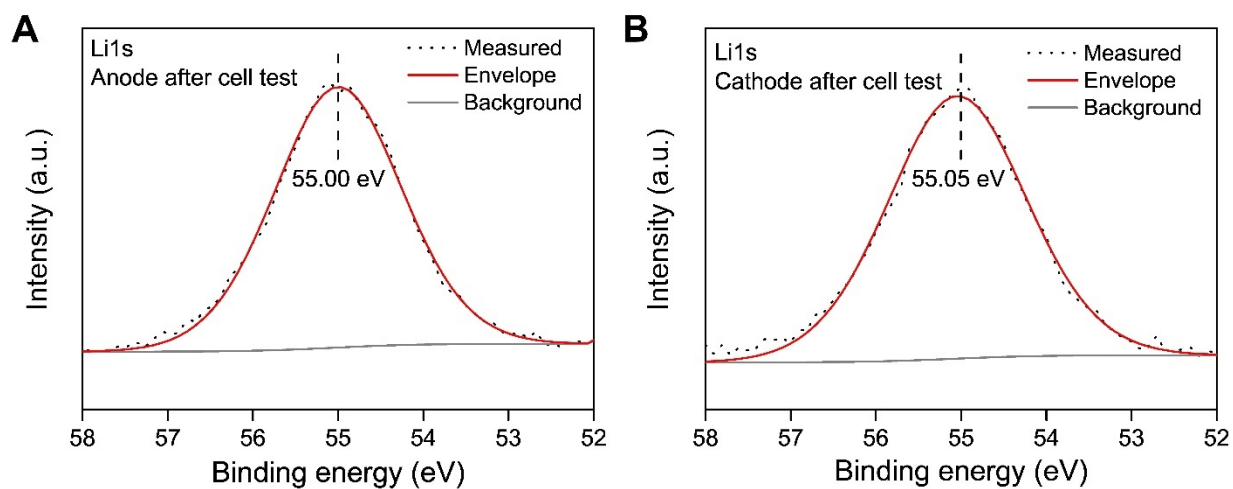


Fig. S9. Li 1s XPS spectra of (A) anode and (B) cathode materials after cell test.

Fig. S10.

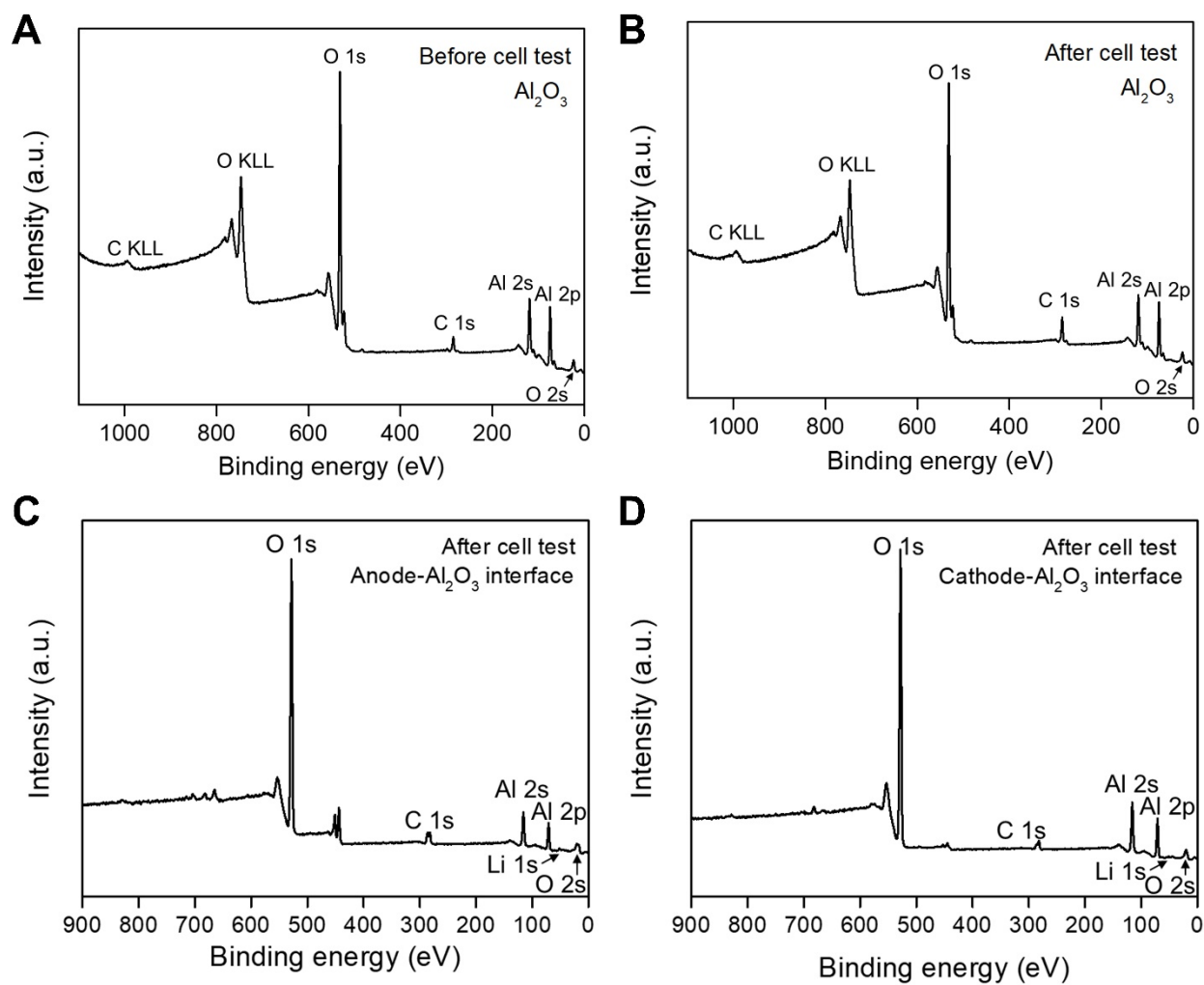


Fig. S10. XPS survey spectra of Al_2O_3 (A) before and (B) after cell test, and (C) anode- Al_2O_3 interface and (D) cathode- Al_2O_3 interface after cell test.

Effect of LiOH on cell performance

LiOH was introduced into the anode (NiO), the middle Al₂O₃ layer, and the cathode (NiO or (La_{0.60}Sr_{0.40})_{0.95}Co_{0.20}Fe_{0.80}O_{3- δ} named as LSCF), respectively. As shown in Table S6, when 30 wt% LiOH was added into the Al₂O₃ layer of the NiO/Al₂O₃/NiO cell, the cell operation with H₂ fuel for its anode and air for its cathode generated zero power density due to no current. This indicates that LiOH didn't contribute to the transfer of protons or O²⁻ ions in the Al₂O₃ layer for the cell. Furthermore, when 25 wt% LiOH was included in the NiO anode, power density was not obtained either. In contrast, the introduction of 25 wt% LiOH into the NiO cathode generated power density of 22 mW/cm². Furthermore, when 33 wt% LiOH was added into the LSCF cathode, the cell generated power density of 89 mW/cm². These reveal that LiOH is necessary in the cathode of the cell. Different from a conventional ceramic proton fuel cell that has a sintered cathode to reduce O₂ to O²⁻ ions and then transfer to the cathode-electrolyte interface for the reaction with protons to H₂O, the WSSFC possessed an un-sintered cathode that suffers the large grain boundary with high resistance for the transfer of O²⁻ ions. Therefore, a LiOH liquid phase or its aqueous solution plays an important role in the cathode of WSSFC, namely, the O²⁻ ions (generated on Ni/NiO active components of the cathode) combine with H₂O to OH⁻ ions which then transfer via LiOH to the interface between cathode and the Al₂O₃ layer to react with protons to H₂O. This explains why a LNCA electrode, which can decompose into not only active components of Ni/NiO but also LiOH, is needed for WSSFCs (**table S6**).

Importantly, the existence of LiOH in the cathode raises concern about whether LiOH may react with CO₂ in air flow to continually form Li₂CO₃ and thus may decrease the performance of the cathode. To clarify it, we examined the cathode by FT-IR spectra. As shown in **fig. S11**, one can see no IR carbonate peak at around 1500 cm⁻¹ for pristine LNCA, whereas the carbonate peak was observed for the cathode at open circuit condition and 550 °C for 2 hours. However, the peak intensity of carbonate is smaller for the cathode at the closed circuit condition than that at the open circuit condition for 2 hours, indicating that the cell operation inhibited the formation of carbonate. Furthermore, the IR peak intensity of carbonate is much smaller for 100 hours of operation than for 2 hours, indicating that the carbonate in the cathode greatly decreased with reaction time. This demonstrated that the formation of Li₂CO₃ in the cathode is not an issue for the cell performance.

Table S6.

Table S6. Effect of LiOH on the performance of WSSFC with H₂ fuel for anode and air for cathode at 550 °C.

Anode	Electrolyte	Cathode	PPD (mW/cm ²)	OCV (V)
NiO	Al ₂ O ₃	NiO	0	0
NiO (25wt% LiOH)	Al ₂ O ₃	NiO	0	0.87
NiO	Al ₂ O ₃ (30wt% LiOH)	NiO	0	0.46
NiO	Al ₂ O ₃	NiO (25wt% LiOH)	22	0.99
NiO	Al ₂ O ₃	LSCF	0	0
NiO (25wt% LiOH)	Al ₂ O ₃	LSCF	0	0.70
NiO	Al ₂ O ₃ (30wt% LiOH)	LSCF	0	0.15
NiO	Al ₂ O ₃	LSCF (33wt% LiOH)	89	0.97

LSCF: (La_{0.60}Sr_{0.40})_{0.95}Co_{0.20}Fe_{0.80}O_{3- δ}

Fig. S11.

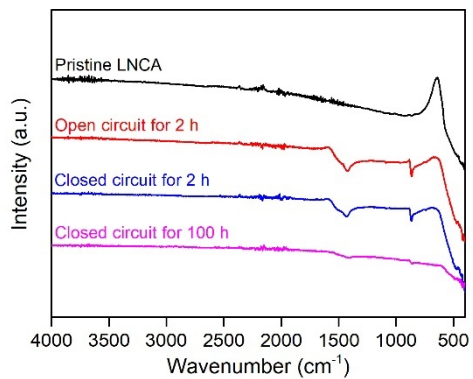


Fig. S11. FTIR spectra of LNCA as the air cathode used in WSSFC at various conditions (pristine LNCA without operation, after 2 hours at open circuit condition and 550 °C, after operation at closed circuit condition (with current density of 72 mA/cm²) and 550 °C for 2 hours, and after operation at closed circuit condition (with current density of 72mA/cm²) and 550 °C for 100 hours, respectively).

Proton conductivity

The protonic conductivity of a ceramic protonic electrolyte is usually determined by electrochemical impedance spectroscopy (EIS) with inert electrodes (such as Au) under wet N₂ atmosphere (S3, S4). This is based on the following principle: the interaction between the oxygen vacancies of the ceramic proton conductor and steam can produce proton ions, leading to the protonic transportation in the conductor (S5, S6). First, we employed this method to determine the protonic conductivity of Al₂O₃ with inert Au electrodes under wet N₂ atmosphere, showing very high area specific resistance of $5.8 \times 10^7 \Omega \text{ cm}^2$ (i.e., very low conductivity of $5.1 \times 10^{-10} \text{ S cm}^{-1}$) (**fig. S12**). This is consistent with the general recognition that intrinsic Al₂O₃ is an ionic insulator. Unlike a ceramic protonic conductor that has rich oxygen vacancies, Al₂O₃ doesn't possess oxygen vacancies and thus cannot generate protons when it is in contact of steam. In contrast, the protonic conductivity of “water-superstructured Al₂O₃” is in-situ and dynamically created during the cell operation, namely, protons generated on the anode transfer to the cathode through the Al₂O₃ surface with water that was in-situ generated. For this reason, we need to determine the proton conductivity under the operation condition for the cell with the symmetric configuration of LNCA/Al₂O₃/LNCA (here LNCA=LiNi_{0.8}Co_{0.15}Al_{0.05}O₂), exhibiting ultrahigh proton conductivity of 0.13 S cm^{-1} at 550 °C (**Fig. 4A**). Obviously, such an in-situ measurement raised an important concern about whether Li ions from the decomposition of the LNCA electrode may contribute to the ionic transfer in the Al₂O₃ layer. However, we experimentally excluded the role of any Li-based compound in the ionic conductivity of the water-superstructured Al₂O₃ layer as follows: To make sure whether Li ions of the electrode entered into the Al₂O₃ layer, we used inductively coupled plasma (ICP) element analysis to determine Li contents in the 5 parts of the tested cell disk: LNCA anode, anode/Al₂O₃ interface, middle Al₂O₃ layer, Al₂O₃/cathode interface, LNCA cathode. The ICP results showed that Li was not found in the middle Al₂O₃ layer, though Li was detected in the anode, cathode, and two interfaces (**Fig. 3F**). Furthermore, the absence of Li in the middle Al₂O₃ layer was further confirmed by EELS and XPS (**Fig. 3H** and **fig. S10**).

Fig. S12.

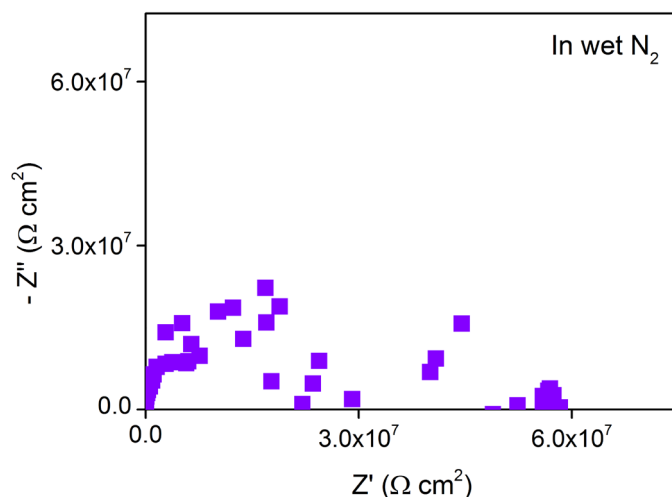


Fig. S12. Impedance spectrum of the Au/Al₂O₃/Au cell in wet N₂ (with 3% H₂O) at 550 °C. It was measured under open-circuit conditions by changing the frequency from 10⁶ to 0.1 Hz. Note: The area specific resistance is at the level of $10^7 \Omega \text{ cm}^2$, revealing that intrinsic Al₂O₃ layer is an ionic insulator with very low conductivity of $5.1 \times 10^{-10} \text{ S cm}^{-1}$.

Fig. S13.

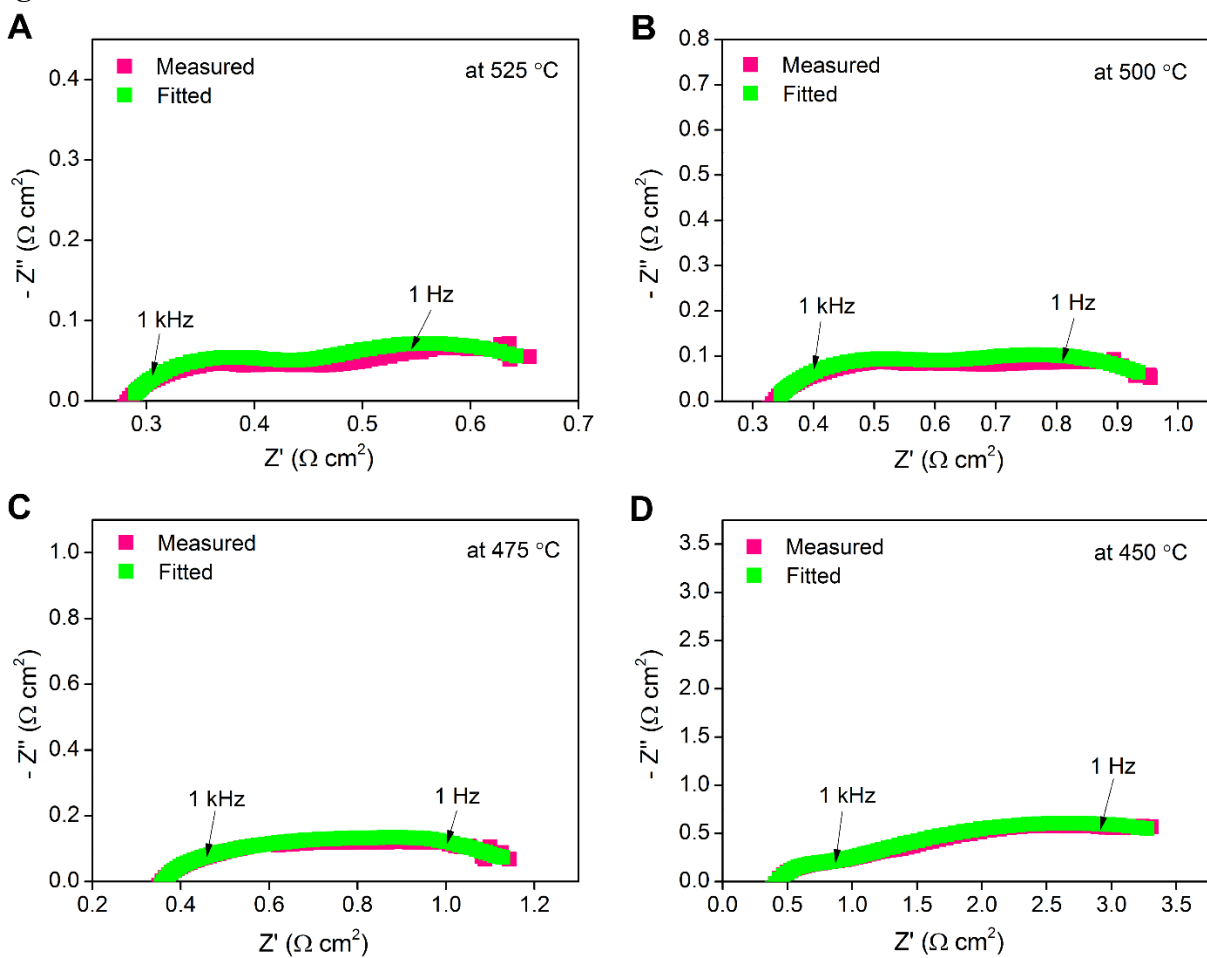


Fig. S13. Impedance spectra of the LNCA/Al₂O₃/LNCA cell under H₂/air open-circuit conditions at various temperatures. It was measured under open-circuit conditions by changing the frequency from 10⁶ to 0.1 Hz. They were fitted with the equivalent circuit of R0(R1||CPE1)(R2||CPE2) (shown by the inset in Fig. 4A).

Table S7.

Table S7. The area-specific ohmic resistances (ASR_{ohm}) obtained from the fitted impedance spectra and corresponding proton conductivities of the water-superstructured Al_2O_3 layer at different temperatures.

Temperature (°C)	450	475	500	525	550
ASR_{ohm} ($\Omega\text{ cm}^2$)	0.42	0.36	0.33	0.28	0.24
Proton conductivity ($S\text{ cm}^{-1}$)	0.07	0.08	0.09	0.11	0.13

Effect of compacting pressure on porosity

Fig. S14.

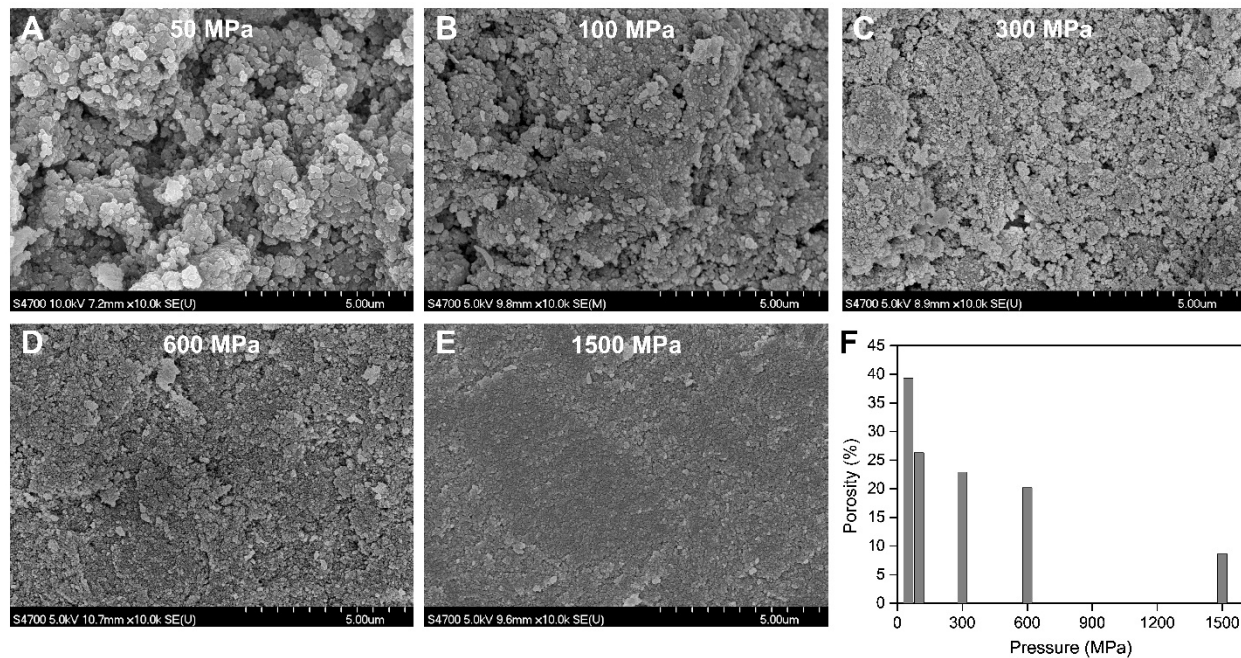


Fig. S14. SEM images of Al₂O₃ layer compacted with different pressures (**A**: 50 MPa, **B**: 100 MPa, **C**: 300 MPa, **D**: 600 MPa, and **E**: 1500 MPa) and their corresponding porosities (**F**).

Fig. S15.

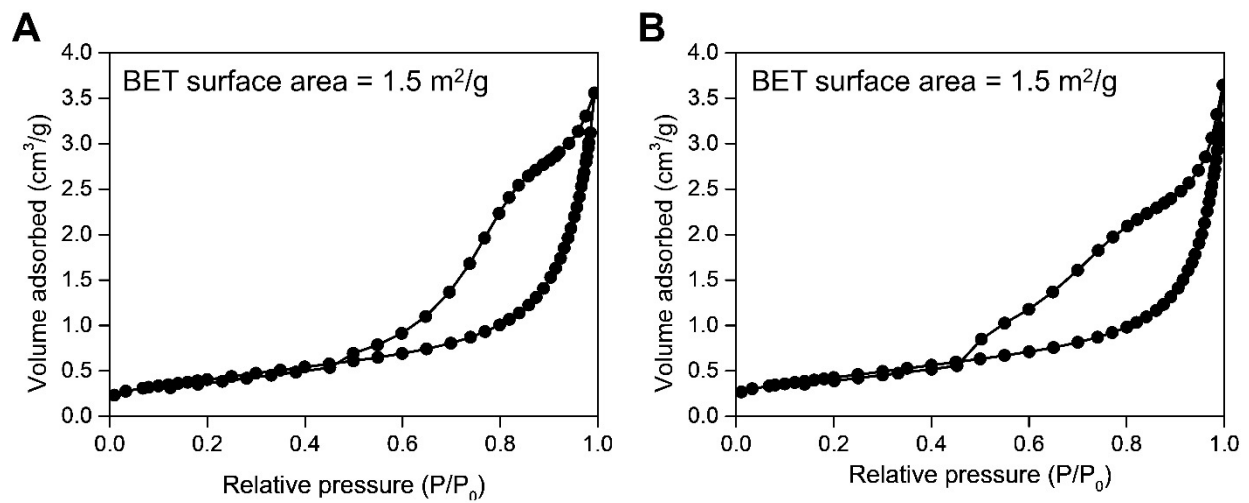


Fig. S15. N₂ adsorption-desorption isotherm curves and BET surface areas of **(A)** LiNi_{0.8}Co_{0.15}Al_{0.05}O₂ (LNCA) powder and **(B)** LNCA pellet (pressed at 100MPa).

Reference

- S1. G. Kresse, D. Joubert, *Phys. Rev. B* **59**, 1758 (1999).
- S2. M. Digne *et al.*, Use of DFT to achieve a rational understanding of acid–basic properties of γ -alumina surfaces. *J. Catal.* **226**, 54–68 (2004).
- S3. J. F. Shin, A. Orera, D. C. Apperley, P. R. Slater, Oxyanion doping strategies to enhance the ionic conductivity in $\text{Ba}_2\text{In}_2\text{O}_5$, *J. Mater. Chem.* **21**, 874–879 (2011).
- S4. A. Satapathy, E. Sinha, B. K. Sonu, S. K. Rout, Conduction and relaxation phenomena in barium zirconate ceramic in wet N_2 environment, *J. Alloys Comp.* **811**, 152042 (2019).
- S5. W. Wang, D. Medvedev, Z. Shao, Gas humidification impact on the properties and performance of perovskite-type functional materials in proton-conducting solid oxide cells, *Adv. Funct. Mater.* **28**, 1802592 (2018).
- S6. D. Han, X. Liu, T. S. Bjørheim, T. Uda, Yttrium-doped barium zirconate-cerate solid solution as proton conducting electrolyte: Why higher cerium concentration leads to better performance for fuel cells and electrolysis cells, *Adv. Energy Mater.* **11**, 2003149 (2021).